Pure Appl. Geophys.

DOI 10.1007/s00024-016-1319-7

Pure and Applied Geophysics

Seismicity on Basement Faults Induced by Simultaneous Fluid Injection–Extraction

Kyung Won Chang[1] and Paul Segall[1]

Abstract—Large-scale carbon dioxide (CO_2) injection into geological formations increases pore pressure, potentially inducing seismicity on critically stressed faults by reducing the effective normal stress. In addition, poroelastic expansion of the reservoir alters stresses, both within and around the formation, which may trigger earthquakes without direct pore-pressure diffusion. One possible solution to mitigate injection-induced earthquakes is to simultaneously extract pre-existing pore fluids from the target reservoir. To examine the feasibility of the injection–extraction strategy, we compute the spatiotemporal change in Coulomb stress on basement normal faults, including: (1) the change in poroelastic stresses $\Delta\tau_s + f\Delta\sigma_n$, where $\Delta\tau_s$ and $\Delta\sigma_n$ are changes in shear and normal stress. respectively, and (2) the change in pore-pressure $f\Delta p$. Using the model of (J. Geophys. Res. Solid Earth *99*(B2):2601–2618, 1994), we estimate the seismicity rate on basement fault zones. Fluid extraction reduces direct pore-pressure diffusion into conductive faults, generally reducing the risk of induced seismicity. Limited diffusion into/from sealing faults results in negligible pore pressure changes within them. However, fluid extraction can cause enhanced seismicity rates on deep normal faults near the injector as well as shallow normal faults near the producer by poroelastic stressing. Changes in seismicity rate driven by poroelastic response to fluid injection–extraction depends on fault geometry, well operations, and the background stressing rate.

Key words: Induced seismicity, basement faults, poroelastic stressing, CO_2 injection, brine extraction.

1. Introduction

Geological CO_2 storage has been proposed to make a significant contribution to the mitigation of climate change by storing gigatonnes of CO_2 into regional scale saline aquifers (Metz *et al.* 2005). The viability of a CO_2 storage project hinges on how much CO_2 can be injected securely into the formation, what is known as storage capacity. A constraint on storage capacity is that elevated pore pressure should not initiate hydraulic fractures in either the storage formation or overlying rocks (Thibeau and Mucha 2011), which could lead to pathways for leakage of injected fluids into overlying aquifers. Even smaller increases in pore pressures, below the threshold for hydraulic fracturing, may cause slip on preexisting faults, potentially triggering small to moderate earthquakes (Zoback and Gorelick 2012). At the In Salah site, where 4 Mt of CO_2 was injected between 2004 and 2011, substantial seismic activity was induced (Verdon *et al.* 2013; Stork *et al.* 2015). For successful operation of geological CO_2 storage, it is critical to understand the physical mechanisms of induced seismicity, and the attendant risks, including: (1) rupture of seals securing storage formations, (2) damage to infrastructure at an operation site, and (3) public concerns raised by felt earthquakes.

Recently, many studies have shown that the disposal of large volumes of wastewater into deep formations contributes significantly to induced earthquakes (Horton 2012; Kim 2013; Kerenan *et al.* 2013; Frohlich *et al.* 2014; Rubinstein and Mahani 2015). These earthquakes can be induced by two types of physical mechanisms: (1) direct increase of pore pressure, and associated decrease in effective confining stress, by fluid diffusion into permeable faults (Healy *et al.* 1968; Raleigh *et al.* 1976; Talwani and Acree 1984; Streit and Hillis 2004; Rutqvist *et al.* 2007; Zoback and Gorelick 2012), and (2) indirect modification of stress fields by poroelastic response to fluid injection (Ellsworth 2013; Segall and Lu 2015; Chang and Segall 2016). This study focuses on induced earthquakes on basement faults due to geological CO_2 storage, since the largest and most damaging earthquakes occur on faults within basement rocks (Horton 2012; Zhang *et al.* 2013; Kerenan *et al.* 2014; Hornbach *et al.* 2015; Chang and Segall 2016).

[1] Department of Geophysics, Stanford University, Stanford, CA 94305, USA. E-mail: k1chang@stanford.edu; segall@stanford.edu

Published online: 02 June 2016

Increased pore pressure has been considered as the primary factor generating induced seismicity (Healy *et al.* 1968; Raleigh *et al.* 1976; Chen and Nur 1992), while the changes in pore pressure are primarily determined by the volume and rate of injected fluid. A possible engineering solution to mitigate injection-induced pore pressure increases is to extract ambient pore fluid from the target formation during injection (Court *et al.* 2011; Bergmo *et al.* 2011). The basic concept of a fluid injection–extraction operation is to balance the fluid mass in the target formation. Several strategies have been suggested to manage injection-induced pressure buildup during geological CO_2 storage: simultaneous extraction with injection (Buscheck *et al.* 2012), brine extraction driven by CO_2 injection (passive extraction) (Bergmo *et al.* 2011), or targeted extraction limiting local pressure buildup (impact-driven pressure management) (Birkholzer *et al.* 2012). These strategies can maintain pore pressure within the target reservoir below the threshold for hydraulic fracturing. Concomitant extraction can allow higher injection rates and/or injection of larger volumes of fluids. The potential storage efficiency is also governed by geological characteristics, including initial and boundary conditions, and well design, including spacing, number, and location (Hosseini and Nicot 2012; Heath *et al.* 2014; Liu *et al.* 2015).

Faulting and seismicity are also associated with fluid extraction, where pore-pressures decline within the reservoir (Segall 1989). Faulting within the reservoir can be produced by the decrease in pore pressure and consequent increase in vertical effective stress (Segall and Fitzgerald 1998). On the other hand, faulting external to the reservoir is understood to result from poroelastic stress changes (Segall 1989; Segall *et al.* 1994). If the changes in shear and/or normal stress are sufficient to overcome the frictional resistance to slip on fault surfaces, we expect seismicity to occur on critically stressed faults.

This modeling study investigates whether fluid extraction from the target reservoir can mitigate injection-induced seismicity along basement faults. Our generic model does not test a particular field-scale scenario for CO_2 injection. Rather, the objective is to understand the physical processes of induced seismicity caused by combined fluid injection–extraction, and to suggests general principals for safe operation of geological CO_2 storage. The goal of this work is to examine the response of different types of basement faults to a generic injection–extraction scenario. Using a fully coupled poroelastic model, we obtain the spatiotemporal evolution of pore pressure and stress and compute the Coulomb stress changes on those faults. We then estimate the seismicity rate given the applied stress history following Chang and Segall (2016). Our analysis suggests that fluid extraction reduces pore pressures and is thus relatively stabilizing. However, extraction itself perturbs the stress field and can reduce fault stability depending on fault orientation, stress state, and production characteristics.

2. Model Problem

We perform numerical studies, including full poroelastic coupling and time-dependent earthquake nucleation, to examine how fluid injection–extraction perturbs the pore pressure and stress fields and affects induced seismicity on basement faults.

2.1. Poroelastic Coupling Model

The linear theory of poroelasticity for an isotropic, fluid-filled porous medium relates the strains ϵ_{ij} and the increment in fluid mass per-unit volume of solid, Δm, to a linear combination of stresses σ_{ij} and pore pressure p (Biot 1941; Rice and Cleary 1976; Wang 2000)

$$2G\epsilon_{ij} = \sigma_{ij} - \frac{\nu}{1+\nu}\sigma_{kk}\delta_{ij} + \frac{(1-2\nu)\alpha}{1+\nu}p\delta_{ij}, \quad (1)$$

$$\Delta m = \frac{9\rho_f(\nu_u - \nu)}{2GB^2(1+\nu)(1+\nu_u)}\left(\frac{B\sigma_{kk}}{3} + p\right), \quad (2)$$

where G (Pa) is the shear modulus, ν (−, dimensionless), ν_u is the Poisson's ratio under drained and undrained conditions, and α (−) is Biot–Willis coefficient relating change in pore pressure to volumetric strain. ρ_f (kg/m^3) is the fluid density, and B (−) is Skempton's coefficient giving the ratio of the change in pore pressure to the change in mean normal stress for undrained conditions ($p = -B\sigma_{kk}/3$).

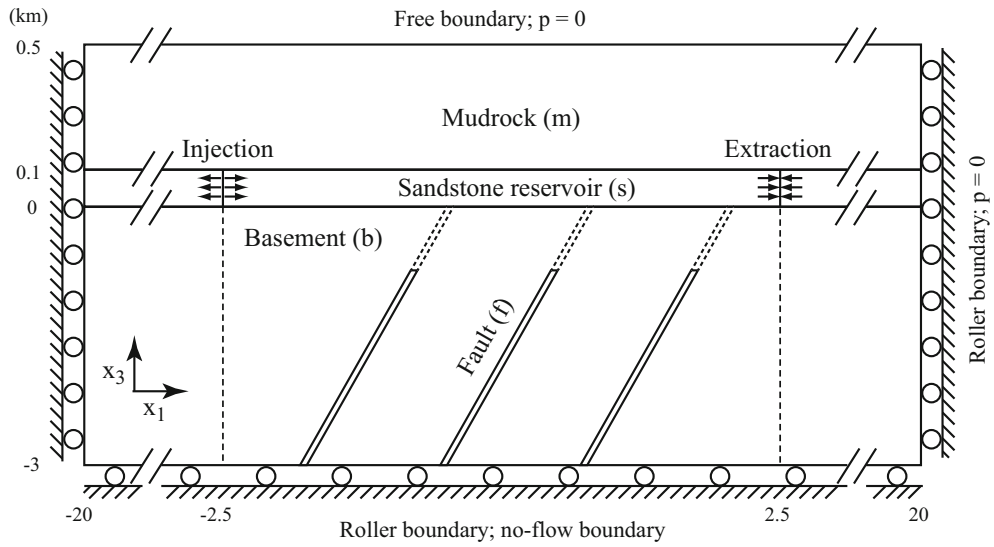

Figure 1
Schematic description of the model. The formation properties are given in Table 1. Laterally and vertically extensive geometry ($L \sim 6\sqrt{4c_s\Delta t}$; $H_b \sim 18\sqrt{4c_b\Delta t}$) minimizes boundary effects on pore pressure. Isolated faults are shown; the upper limits of the faults are extended to $x_3 = 0$ for faults connected to the sandstone reservoir

Combining the two constitutive Eqs. (1) and (2) with field equations for conservation of momentum and fluid mass yields the governing equations of poroelasticity. The force equilibrium equation describing rock deformation can be expressed in terms of displacement u_i and pore pressure p (e.g. Segall 2010)

$$\nabla \cdot [G(\mathbf{x})\nabla \mathbf{u}] + \nabla\left[\frac{G(\mathbf{x})}{1-2\nu(\mathbf{x})}\right]\nabla \cdot \mathbf{u} - \alpha(\mathbf{x})\nabla p + \mathbf{f} = 0, \tag{3}$$

where $\mathbf{f}$ are body forces per-unit volume. Equation (3) shows that pore-pressure gradients act as body forces, and thus induce deformation of the solid. The flow equation for single-phase transient flow in a heterogeneous and isotropic compressible porous medium can be written in the form of an inhomogeneous diffusion equation for pore pressure p by combining the fluid mass change (2), Darcy's law $\mathbf{q} = -(\rho_f \kappa/\eta)\nabla p$, where κ (m^2) is permeability, η (Pa·s) is the fluid viscosity, and fluid mass conservation equation (Wang 2000; Segall 2010)

$$S_\epsilon(\mathbf{x})\frac{\partial p}{\partial t} - \frac{1}{\eta}\nabla \cdot [\kappa(\mathbf{x})\nabla p] = -\alpha(\mathbf{x})\frac{\partial}{\partial t}(\nabla \cdot \mathbf{u}) + Q(x,t), \tag{4}$$

where Q is the volume of fluid added from an external source (per-unit bulk volume per-unit time).

Here, S_ϵ (Pa^{-1}) is the constrained specific storage (Wang 2000), which represents the fluid volume change (per-unit control volume) due to pressure change while holding the control volume constant, given by

$$S_\epsilon = \frac{\alpha^2(1-2\nu)(1-2\nu_u)}{2G(\nu_u - \nu)}. \tag{5}$$

In Eq. (4), the divergence of the displacements acts as a source term. Note that full poroelastic coupling is defined by the presence of ∇p in the equilibrium equation (3) and $\nabla \cdot \mathbf{u}$ in the flow equation (4).

We model a three-layer formation comprising a laterally extensive sandstone reservoir ($L = 40$ km; $H_s = 0.1$ km) overlain by a thick mudrock (shale, siltstone, or fine-grained clastic rock) sequence ($H_m = 0.5$ km) and underlain by basement rocks ($H_b = 3$ km), including faults, as shown in Fig. 1. The two-dimensional (2D) plane strain domain has origin at the bottom center of the sandstone reservoir. The spatial variation of the physical properties in this layered geometry is given by

$$\kappa(\mathbf{x}) = \begin{cases} \kappa_m; & x_3 > H_s \\ \kappa_s; & 0 \le x_3 \le H_s \\ \kappa_b; & x_3 < 0 \end{cases}, \tag{6}$$

Table 1

Summary of model properties

Model properties	Mudrock[a]	Sandstone[a]	Basement[b]	Fault[b]	Fluid
κ^c (m^2)	1×10^{-19}	6.4×10^{-14}	2×10^{-17}	1×10^{-13}, 1×10^{-21}	–
ϕ (-)	0.1	0.25	0.05	0.02	–
G (GPa)	11.5	7.6	25	6	–
v (-)	0.3	0.15	0.2	0.2	–
v_u (-)	0.35	0.25	0.25	0.33	–
B (-)	0.8	0.62	0.85	0.62	–
c (m^2/s)	6.4×10^{-6}	7.4×10^{-1}	2.7×10^{-3}	8.3×10^{-1}, 8.3×10^{-9}	–
f (-)	0.5	0.6	0.6	0.75	–
C (MPa)	75	80	130	0	–
ρ (kg/m^3)	2600	2500	2740	2500	1000
η (Pa·s)	–	–	–	–	1×10^{-3}

[a] Mudrock and sandstone properties are based on Kim and Hosseini (2013).

[b] Hydrological properties of basement and faults are based on tabulation in Zhang *et al.* (2013), and mechanical properties are based on Stanislavsky and Garven (2002); Willson *et al.* (2007).

[c] Fault permeability varies for conductive or sealing fault

$$S_\epsilon(\mathbf{x}) = \begin{cases} S_{\epsilon,m}; & x_3 > H_s \\ S_{\epsilon,s}; & 0 \le x_3 \le H_s \\ S_{\epsilon,b}; & x_3 < 0 \end{cases}, \tag{7}$$

where the subscripts m, s, and b represent each sequence of mudrock, sandstone, and basement rock, and hydrological and mechanical properties of each layer are given in Table 1.

We include a set of normal faults with dip angle $\theta = 60^\circ$ within the basement to investigate the poroelastic effect of the injection–extraction operation on the perturbation in stresses and pore pressure acting on pre-existing faults (Fig. 1). Three different types of faults are implemented depending on fault permeability ($\kappa_f/\kappa_b = 5 \times 10^3$ for conductive or $\kappa_f/\kappa_b = 5 \times 10^{-5}$ for sealing) and hydraulic connectivity between basement faults and the target reservoir (isolated or connected): (1) conductive/isolated faults, (2) conductive/connected faults, and (3) sealing/connected faults. The properties of the fault zones are given in Table 1.

We consider 2D plane strain conditions ($\partial(\cdot)/\partial x_2 = 0$) with origin at the bottom of the reservoir midway between the two wells. Fluid is injected (extracted) into (from) a sandstone reservoir simultaneously at a constant mass rate of 0.3 kg/m s per-unit length of the reservoir thickness at $x_1 = \pm 2.5$ km for $\Delta t = 30$ days. To investigate post shut-in poroelastic response of the formation to the fluid injection–extraction operation, the numerical simulation runs for 500 days. The initial conditions for stress and pore-pressure perturbations are

$$\sigma_{ij}(\mathbf{x}, t = 0) = 0, \tag{8}$$

$$p(\mathbf{x}, t = 0) = 0. \tag{9}$$

The hydraulic boundary conditions are given by

$$\lim_{x_1 = \pm L/2} \lim_{x_3 = +H_m} p = 0, \tag{10}$$

$$\lim_{x_3 = -H_b} \hat{n} \cdot \nabla p = 0. \tag{11}$$

For the bottom boundary, we assume that the basement rocks are underlain by impermeable sequences. Although we use finite-element modeling with finite boundaries, the boundary effects on diffusion are minimized due to the laterally and vertically extensive geometry compared to the characteristic diffusive length in each direction, defined by the hydraulic diffusivity of the formation $c = \kappa/\eta S$ and injection duration Δt. The lateral distance from either well to the outer boundary is about six times the characteristic diffusive length in the sandstone reservoir ($L_w = 17.5$ km $\sim 6x_{c,1}$, where

$x_{c,1} = \sqrt{4c_s\Delta t}$), while the thickness of the basement is about 18 times the characteristic length in the basement ($H_b = 3$ km $\sim 18x_{c,3}$, where $x_{c,3} = \sqrt{4c_b\Delta t}$). Note that longer injection periods or higher injection rates, as proposed for field-scale CO_2 storage projects, require larger model domains to neglect boundary effects. The no-flow boundary at the bottom can limit vertical diffusion through conductive/connected faults, which may cause lateral diffusion into the surrounding basement rocks and subsequent poroelastic stress changes within the basement. However, the diffusivity contrast between conductive faults and basement rocks ($c_b/c_f \sim 0.002$) minimizes lateral diffusion, such that fault stability is dominated by vertical diffusion along the fault zone.

Mechanically, the top boundary is traction-free, and the bottom and side boundaries are fixed in the normal direction to boundaries, but free to move in the parallel direction (so-called roller boundary condition) given by

$$\lim_{x_j \to \infty} \hat{n} \cdot \mathbf{u} = 0, \tag{12}$$

where $\hat{n}$ is the normal vector, and $\mathbf{u}$ is displacement.

2.2. Single-Phase Flow Model

The difference between the hydrological and mechanical properties of ambient pore fluids and supercritical CO_2 needs to be addressed, because the increase in total mobility ($\lambda_T = \lambda_g + \lambda_l$ where $\lambda_i = k_{ri}/\mu_i$ is the mobility of phase i defined by the ratio of relative permeability to viscosity of phase i, g for CO_2 and l for the formation fluid) with increasing saturation of low-viscosity CO_2 ($\mu_g = 1 \times 10^{-4}$ Pa s) will reduce pore-pressure buildup within the region directly invaded by CO_2, specifically near the injector. However, we focus on pore-pressure perturbations outside the region directly invaded by CO_2, beyond the effect of multiphase flow, where the pressure disturbance created by single- and two-phase flow will be similar (Nicot *et al.* 2009; Chang *et al.* 2013). This implies that single-phase pressure is a good approximation for the pressure evolution beyond the two-phase region.

To verify the single-phase approximation, we estimate the lateral extent of the CO_2 plume using a solution in the Buckley–Leverett form (Buckley and Leverett 1942)

$$r_s = \frac{QB_g\Delta t}{\rho_g \phi}\left(\frac{df_g}{dS_g}\right)_{S_{gf}}, \tag{13}$$

where r_s is the location of the CO_2-saturated front, B_g (m^3/m^3) is the formation volume factor for CO_2 ($B_g = 0.00291$ m^3/m^3), ρ_g is CO_2 density ($\rho_g = 600$ kg/m^3 at and average reservoir pressure of 16 MPa and temperature 60 °C), S_g is CO_2 saturation, and $f_g = \lambda_g/\lambda_T$ is the fractional flow function, which measures the CO_2 fraction of the total flow. The derivative df_g/dS_g evaluated at the front saturation S_{gf} is determined by the tangent construction (Welge *et al.* 1962), with mean value of 3.47 from the data for relative permeability of sandstone reservoirs that are candidate CO_2 storage sites in onshore North American sedimentary basins (Bennion and Bachu 2005). The corresponding estimate of the location of the saturation front after 30 day injection is 0.05 km ($r_s \ll x_{c,1}$), such that the pressure "front" propagates much further than the saturation front within the sandstone reservoir. For the vertical flow of CO_2 into bounding sequences, low-permeability basement rocks inhibit downward migration of CO_2 plumes during injection. In addition, the less dense CO_2 tends to invade the overlying strata, not the basement, after shut-in. The single-phase approach, therefore, is a reasonable approximation for understanding the mechanism of induced seismicity on basement faults.

2.3. Seismicity Rate Prediction

From the full poroelastic coupling model, we obtain the spatiotemporal evolution of the Coulomb stress $\tau = \tau_s + f(\sigma_n + p)$, where τ_s and σ_n are shear and normal stresses resolved on the faults, and f is the fault friction coefficient. For moderate changes in $\tau_s/\bar{\sigma}$, where $\bar{\sigma} = \sigma_n + p$ is the effective stress, we compute the seismicity rate from the model of Dieterich (1994) and Segall and Lu (2015)

$$\frac{dR}{dt} = \frac{R}{t_a}\left(\frac{\dot{\tau}}{\dot{\tau}_0} - R\right), \tag{14}$$

where R is the seismicity rate relative to the steady-state seismicity rate at reference stressing rate $\dot{\tau}_0$, and $t_a \equiv A\bar{\sigma}/\dot{\tau}_0$ is characteristic decay time. In this study, we assume the constitutive parameter $A = 0.001$ quantifying the direct effect on slip rate in the rate-

state friction law and the effective normal stress acting on the fault plane $\bar{\sigma} = 10$ MPa at a depth of about 1 km. The background stressing rate $\dot{\tau}_0$ is assumed to be 2×10^{-4} MPa/years, such that a typical 0.2 MP stress drop accumulates in 10^3 years. This leads to a characteristic time $t_a = 50$ years. We solve the ordinary differential equation (14) to obtain $R(\mathbf{x}, \mathbf{t})$ along the basement faults using the `Matlab` solver `ode45` with relative tolerance of `1e-6` and very small absolute tolerance. We obtain $\dot{\tau}$ using the (analytical) time derivative of a spline curve fit to the Coulomb stress at discrete time steps ($t_{step} = 0.1$ years) from the finite-element method (FEM) calculations. The details of the numerical procedure are found in Chang and Segall (2016).

3. Numerical Results

We perform numerical simulations of the poroelastic model defined by the governing Eqs. (3) and (4), the parameter fields (6) and (7), initial and boundary conditions (8−12) to study the perturbation in pore pressure and stresses driven by fluid injection–extraction. The finite-element analysis is conducted with COMSOL Multiphysics (2014) using bilinear quadrilateral elements for spatial discretization (Hughes 2000) and a variable step method for time integration (Dreij *et al.* 2011). The numerical mesh is highly refined near the upper and lower boundaries of the sandstone reservoir as well as the basement faults to resolve the strong pressure gradients typical for these problems.

3.1. Pore-Pressure Perturbation

We begin by illustrating the effect of fluid extraction on the perturbation in pore pressure. Figure 2a shows the temporal evolution of the pressure "front" r_f, defined by an arbitrary cutoff value of $\Delta p = 1$ MPa within the sandstone reservoir on a log–log plot. Note that r_f addresses only the extent of the pore-pressure disturbance, not the peak pore-pressure change. We compare the results from two types of well operations: (1) injection only (red line) and (2) simultaneous injection and extraction (blue line). The dash line represents the end of well operations at $\Delta t = 30$ days at which we obtain the so-called radius of review, $r_{f,inj} \equiv r_f(t = \Delta t)$. Each dot denotes r_f for $t = 10, 30, 110$, and 200 days shown with the green contours in Fig. 2b–e for the injection-only operation and Fig. 2f–i for simultaneous injection and extraction.

We examine the post shut-in propagation of the pressure "front" and obtain the maximum radius of review, $r_{f,max} \equiv max(r_f)$. Our results show that $r_{f,max}$ approaches ~ 3.7 km from the injector after $t_{max} = 110$ days ($r_{f,max} = 1.8 \times r_{f,inj}$ and $t_{max} = 2.7 \times \Delta t$; point d in Fig. 2a). Then, the pressure "front" recedes as pore pressure relaxes back to an equilibrium state (point e in Fig. 2a).

Simultaneous extraction reduces pore-pressure buildup within a target reservoir, limiting the extent of the pressure "front" ($r_{f,inj} = 1.9$ km) compared to the injection-only operation (point g in Fig. 2a). Subsequently, a smaller maximum radius of review is obtained within a shorter period, $r_{f,max} \sim 2.0$ km at $t_{max} = 37.5$ days ($r_{f,max} = 1.1 \times r_{f,inj}$ and $t_{max} = 1.3 \times \Delta t$) after shut-in. Note that the retardation of the pressure front depends on well operations (distance between wells, time, and rate) and reservoir diffusivity. Longer injection–extraction times may result in larger deviations in the magnitudes of $r_{f,inj}$ and $r_{f,max}$ due to stronger interference between wells with time. Assuming that the volume extracted balances the volume injected, a steady-state solution may be obtained with sufficiently long period of injection–extraction.

When the reservoir is underlain by basement rocks, the low, but non-zero, permeability of the basement allows downward diffusion of pore pressure. Such pore-pressure dissipation may enhance the storage capacity of the formation and decrease the radius of review. However, the basement may contain critically stressed faults that can be destabilized by perturbations in pore pressure and stress. Figure 2b–i shows pore-pressure perturbations in the formation, including conductive/isolated basement faults. The response of the basement faults to injection depends on the spatiotemporal distribution of pore pressure and stress, which in turn is controlled by the basement rock properties as well as injection. After shut-in, pore pressure continues to diffuse and

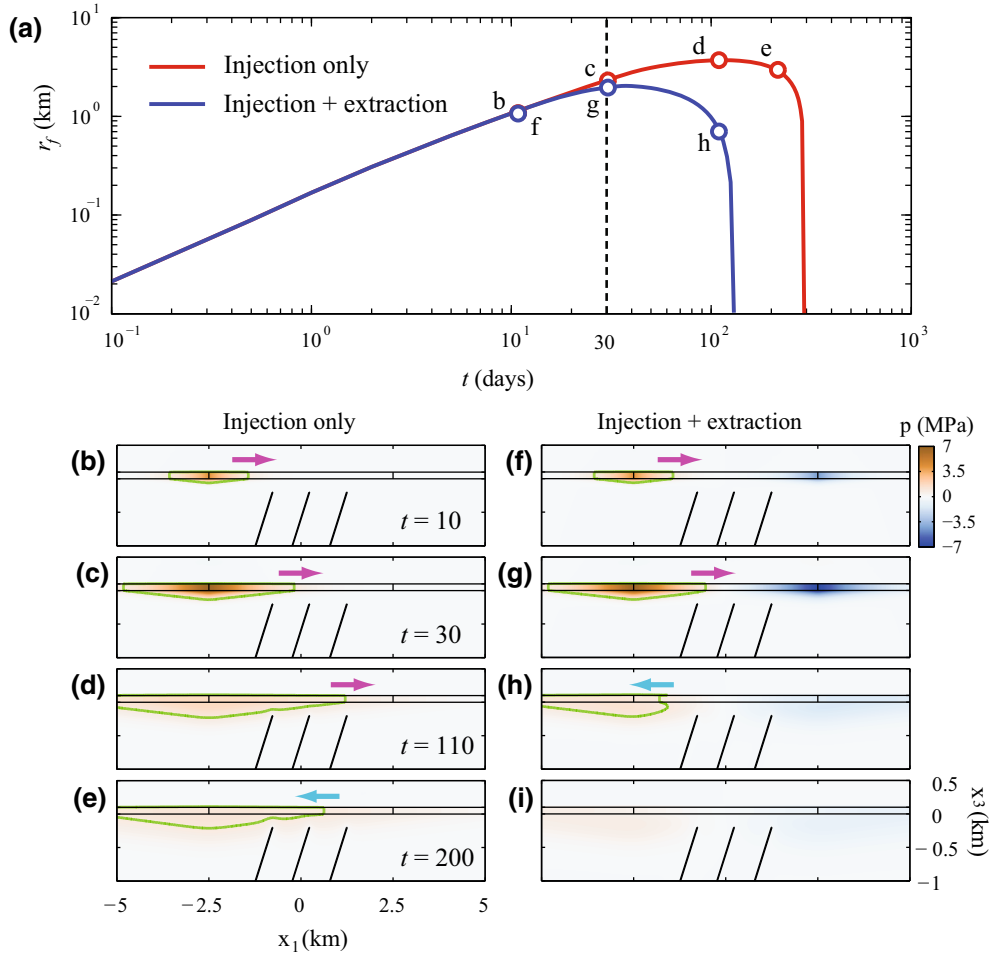

Figure 2

a The location of the pressure "front" within the target reservoir during and after well operations. *Dash line* indicates the end of injection operation ($\Delta t = 30$ days). Pore-pressure profiles at $t = 10, 30, 110$, and 200 days for two different well operations: **b–e** injection-only and **f–i** injection–extraction. A series of *dots* on *plots* in **a** match with the location of the pressure "front" of 1 MPa at each time step shown as a *green line* within the target reservoir shown in **b–i**

eventually approaches the basement faults (Fig. 2d–e). Local pressure gradients into the conductive faults are strong enough to cause faster pressure diffusion, which distorts the pressure contour. Changing the basement permeability will change the time it takes the pressure disturbance to approach the faults isolated from the reservoir. For hydraulically connected faults, strong diffusion still develops along the faults during injection, as long as the faults are much more conductive than the basement (Chang and Segall 2016). Higher basement permeability may allow more lateral diffusion into the surrounding basement from the pressurized fault after shut-in. This result emphasizes that monitoring post shut-in enlargement of the pressurized zone in both the lateral and vertical directions is required to guarantee formation stability.

Fluid extraction reduces pore-pressure diffusion into the basement, and thus a smaller perturbation in pore pressure is observed on the fault near the injection well (Fig. 2h–i). Furthermore, the zone of depleted pore pressure penetrates into the fault near the extraction well, which actually acts to stabilize this structure.

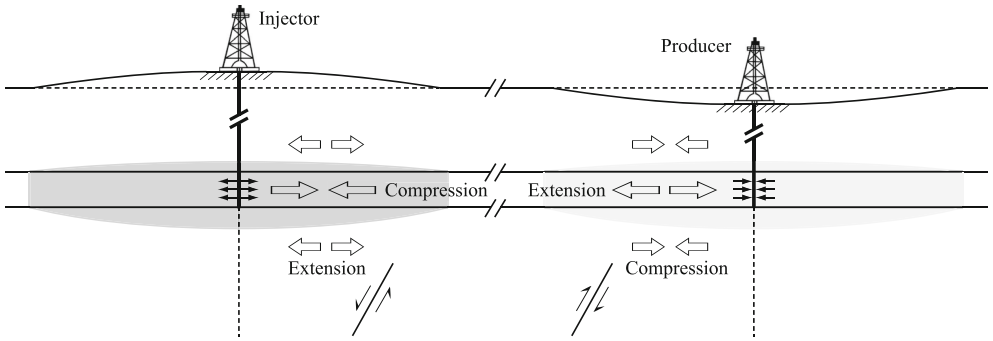

Figure 3
Schematic description summarizing formation deformation and faulting associated with fluid injection–extraction. *Open arrows* indicate *horizontal strains* in the formation. The (*lighter*) *gray* region indicates (de)pressurized zones due to direct pore-pressure diffusion. Poroelastic extension of basement rocks near injector enhances normal faulting, while compression near producer favors reverse faulting

3.2. Poroelastic Stressing in the Basement

Our results show that simultaneous injection–extraction may be one of the engineering options to mitigate injection-induced pore pressure in the target reservoir and retard direct diffusion into basement faults (refer to Fig. 2h–i). Poroelastic stresses, however, are transmitted to deep formations, potentially destabilizing faults even without elevated pore pressure (Chang and Segall 2016). Therefore, it is important to examine poroelastic stress changes acting on basement faults, in addition to the impact of direct pore-pressure changes.

Before presenting numerical results, we illustrate how the poroelastic response to fluid injection–extraction perturbs stress fields in both the formation and basement. Figure 3 describes schematically the sign of poroelastic deformation associated with well operations. [The poroelastic response to fluid injection alone is described in Chang and Segall (2016)]. Near the producer, extension develops within the depressurized region due to the poroelastic response to pore-pressure depletion. Reduced pore pressures within the reservoir cause the reservoir to shrink. This shrinkage induces the horizontal compression of basement rocks below the region of significant pore-pressure decrease (Segall 1989). The opposite effect occurs near the injector with horizontal extension in the basement beneath the injector well. Without direct diffusion of pore pressure, poroelastic effects perturb the stress state on basement faults at depth. The boundary between extensional and compressional environments will be determined by the diffusion of pore pressure and thus the hydraulic properties of the formations. In a background compressional environment, reverse faults near the producer are favored to slip due to increased compression of the basement rocks. In contrast, in a background extensional environment, poroelastic stressing may destabilize normal faults beneath an injection well. In summary, the full poroelastic response to injection–extraction depends on the fault location and orientation, as well as the permeability and hydraulic connectivity to the reservoir.

We compute the change in Coulomb stress produced on a fault plane, assuming a constant friction coefficient f, given by

$$\Delta\tau(t) = [\Delta\tau_s(t) + f\Delta\sigma_n(t)] + f\Delta p(t), \qquad (15)$$

where $\Delta\tau$ is the static change of Coulomb failure stress, $\Delta\tau_s$ is the change in shear stress acting on the fault, $\Delta\sigma_n$ is the change in normal stress on the fault, and Δp is the change in pore pressure. The Coulomb stress change is rearranged in terms of changes in poroelastic stress and pore pressure to investigate the poroelastic response relative to the direct pore-pressure effect, $f\Delta p$. Positive $\Delta\tau$ implies that the fault plane is brought closer to failure; positive $\Delta\tau_s$ indicates that the change in shear stress favors slip on the fault; positive $\Delta\sigma_n$ indicates an increase in tension (decrease in fault normal compression). Note that uncoupled models assume the Coulomb stress change is only a function of change in pore pressure $f\Delta p$,

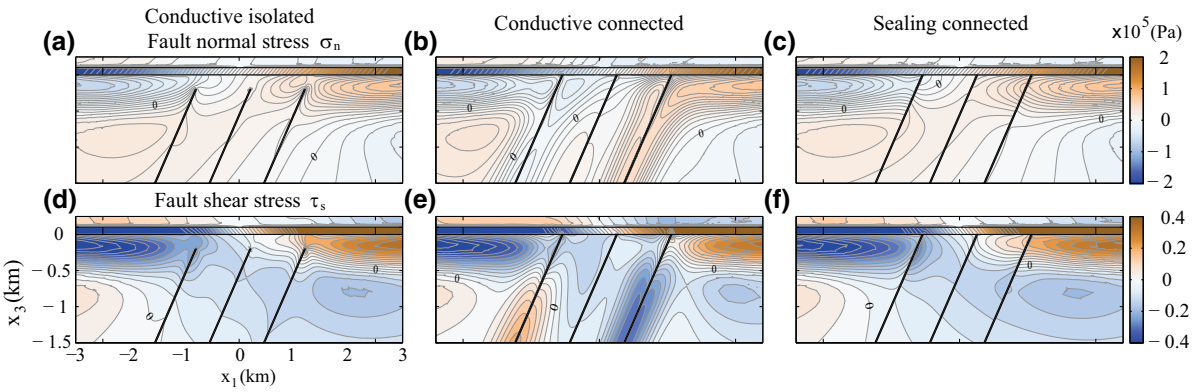

Figure 4
Normal and shear stresses, $\sigma_n(\mathbf{x})$ and $\Delta\tau_s(\mathbf{x})$, at $t = 200$ days with the injection–extraction operation for three types of basement faults: (*left column*) conductive/isolated fault, (*middle column*) conductive/connected fault, and (*right column*) sealing/connected fault

such that shear and normal stresses remain constant with time.

Figure 4 shows the spatial distribution of normal and shear stresses, $\sigma_n(\mathbf{x})$ and $\tau_s(\mathbf{x})$, at $t = 200$ days given the fault orientation in Fig. 1, and assuming the background stress state favors normal faulting. Near the injector, compressive stress ($\sigma_n < 0$) is observed in the shallow basement, as well near the fault zone for the conductive/connected case, where direct diffusion of pore pressure causes the rock volume to increase, inducing compression (Fig. 4a–c; top row). On the other hand, extensional stress ($\sigma_n > 0$) occurs in the deep basement, for either isolated or sealing faults, due to injection-induced lateral expansion of the reservoir formation. Near the producer, fluid extraction results in the opposite behavior within the basement, relative tension in the depleted zone as pore-pressures decline, and compression in the deeper basement due to contraction of the reservoir.

Injection-induced lateral extension, resulting from poroelastic dilation of the target reservoir, causes normal sense of shear ($\tau_s > 0$) on deep basement rocks near the injector (Fig. 4d–f; bottom row). On the other hand, production-induced lateral compression causes reverse sense of shear ($\tau_s < 0$) outside the depleted region near producer. This result implies that fluid extraction may enhance fault stability, even without depletion, for normal faults beneath the producing zone. For conductive/connected faults (Fig. 4e), larger magnitude shear stress is observed along the faults depending on the proximity to the injector (producer) because, rapid pore-pressure diffusion causes pore-pressure gradients outward (inward) the fault zone which must be compensated by stress gradients (Chang and Segall 2016).

Fig. 5a–c (top row) shows the change in the poroelastic stresses, $\Delta\tau_s(\mathbf{x}) + \mathbf{f}\Delta\sigma_\mathbf{n}(\mathbf{x})$, at $t = 200$ days for each fault type. In regions of elevated (depleted) pore pressure, i.e. relatively shallow depths, poroelastic stresses tend to inhibit (favor) normal faulting, given this geometry. On deeper basement rocks, dilation (shrinkage) of the reservoir formation causes increases (decrease) in both $\Delta\sigma_n$ and $\Delta\tau_s$ (refer to Fig. 4), leading to a positive (negative) poroelastic stress change near the injector (producer).

Fig. 5d–f (middle row) shows the change in pore pressure, $f\Delta p(\mathbf{x})$. Within zones of direct pore-pressure diffusion, $|f\Delta p|$ is roughly one order of magnitude larger than $|(\Delta\tau_s + f\Delta\sigma_n)|$, and pore pressure changes control the fault stability, while outside the zone of significant pore-pressure change poroelastic stresses dominate.

Fig. 5g–i (bottom row) shows the total change in Coulomb stress $\Delta\tau(\mathbf{x})$, summing the direct diffusion and poroelastic terms in (15). For the most part, the profile of $\Delta\tau(\mathbf{x})$ is similar to that of $f\Delta p(\mathbf{x})$ (refer to Fig. 5d–f), such that direct pore-pressure diffusion dominates fault stability. For deep isolated or sealing faults, however, small changes in Coulomb stress

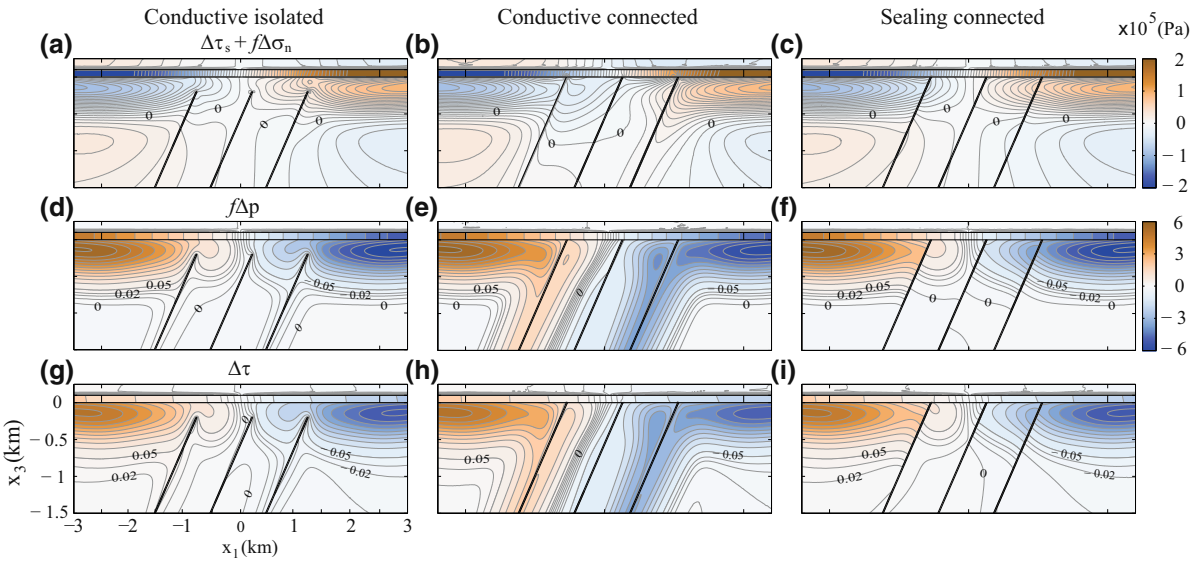

Figure 5
Changes in poroelastic stresses $\Delta\tau_s(\mathbf{x}) + \mathbf{f}\Delta\sigma_\mathbf{n}(\mathbf{x})$, pore pressure $f\Delta p(\mathbf{x})$, and Coulomb stress $\Delta\tau(\mathbf{x})$ at $t = 200$ days with the injection–extraction operation for three types of basement faults

solely by poroelastic stressing may destabilize the faults if they are near critically stressed.

Note that the sign and magnitude of poroelastic effects depend on fault geometry (location, dip, and/or width), well operations (well type, duration, and/or rate), and poroelastic parameters. However, our goal is not to catalog all possible scenarios. Rather, it is to explore general processes and to emphasize that indirect transfer of poroelastic stresses may destabilize basement faults ("poroelastic stressing"), even without direct pore-pressure diffusion into conductive faults hydraulically connected to the target reservoir. General insight into effects of expansion of the reservoir can be gained by consideration of Fig. 3.

We plot the Coulomb stress change $\Delta\tau(t)$ along the middle of the fault (indicated by the orange lines) in Fig. 6; nearest the injector in Fig. 6a–c (left column) while nearest the producer in Fig. 6d–f (right column). The upper limit is the boundary between the reservoir and the basement located at $x_3 = 0$ km, while the lower limit is at $x_3 = -2$ km. The dash line in each subplot of $\Delta\tau$ represents the end of well operations at $\Delta t = 30$ days.

For conductive/isolated faults (Fig. 6a, d), $\Delta\tau$ is positive (negative) above $x_3 = -0.2$ km, in the unfaulted basement near the injector (producer), due to pore-pressure diffusion. At greater depths, there are relatively small changes in $|\Delta\tau|$, following shut-in when poroelastic stressing dominates the Coulomb stress change. Injection-induced extension of the formation causes positive $\Delta\tau$ (Fig. 6a) on the fault near the injector, while production-induced compression results in negative $\Delta\tau$ in the fault zone near the producing well (Fig. 6d). Post shut-in diffusion into/from the fault zones contributes to a gradual increase in $|\Delta\tau|$ along the fault.

For conductive/connected faults (Fig. 6b, e), rapid pore-pressure diffusion dominates the distribution of $\Delta\tau$, in that $|\Delta\tau_s + f\Delta\sigma_n| \ll |f\Delta p|$, resulting in large magnitudes of $|\Delta\tau|$ along the fault zones. The direct pore-pressure effect is destabilizing near the injector and stabilizing near the producer, as expected from the standard theory.

For sealing faults (Fig. 6c, f), low-permeability inhibits pore-pressure diffusion into the faults, so that $|\Delta\tau_s + f\Delta\sigma_n| \gg |f\Delta p|$. On shallow fault zones, nearest the reservoir, pore pressure diffuses into (out of) the surrounding basement rocks causing compression (extension) of the faults, resulting in decreases (increases) in the local Coulomb stress nearest the

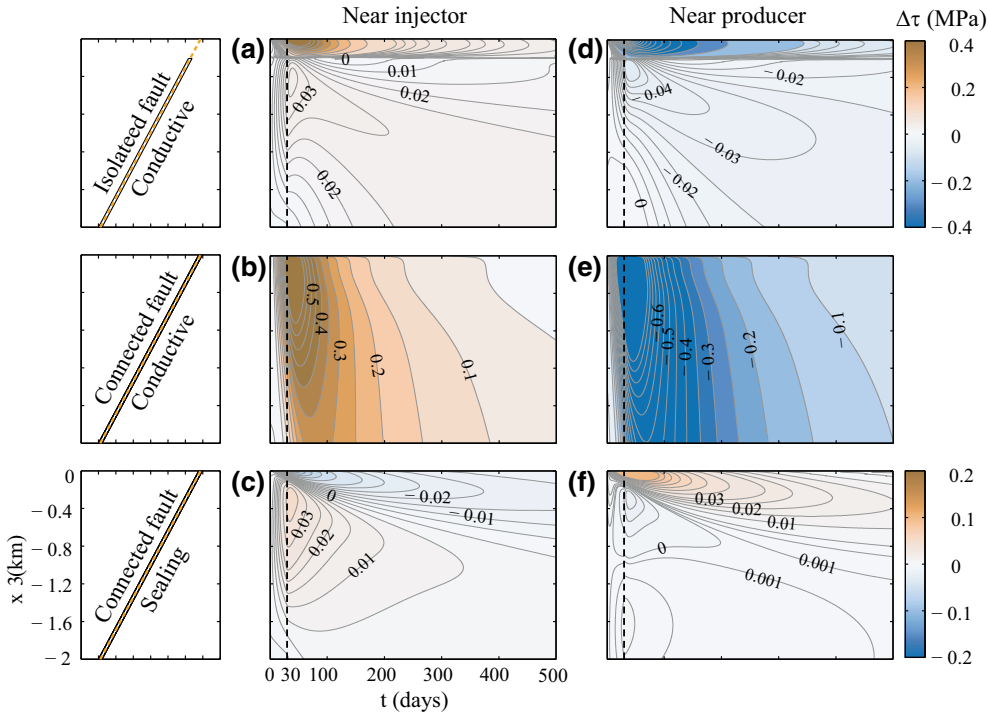

Figure 6
Coulomb stress change $\Delta\tau(t)$ in the middle of the faults near (**a**–**c**) injector and (**d**–**f**) producer: **a**, **d** conductive/isolated fault, **b**, **e** conductive/connected fault, and **c**, **f** sealing fault. Fault geometries are shown in a *left column*; stresses computed along *dashed orange lines*

injector (producer). On the other hand, on deep fault zones, poroelastic dilation (contraction) of the formation due to fluid injection (extraction) results in the Coulomb stress change with opposite signs. This result shows that poroelastic stressing can stabilize or destabilize sealing faults depending on adjacent basement properties, well type, and background stress state. For a normal faulting stress state, injection is destabilizing, while extraction is stabilizing.

3.3. Seismicity Rate Along Basement Faults

We estimate the seismicity rate along the fault zones from the seismicity rate model (14), assuming that earthquakes will not occur on the unfaulted basement ($-0.2 < x_3 < 0$ km, for isolated faults). Figure 7 shows the distribution of the seismicity rate, $\log_{10} R(\mathbf{x}, \mathbf{t})$, on the basement faults nearest either the injection or production well for three cases. The dash line in each plot represents the end of well operations ($\Delta t = 30$ days). As a reference, we model injection-only scenarios with the same types of basement faults (Fig. 7a–f; top two rows), which highlights the effect of fluid extraction on the seismicity (Fig. 7g–l; bottom two rows). Without the extraction well, we observe considerable seismicity on the basement fault far from the injector, particularly for the conductive/connected fault, with a delayed onset, due to longer diffusive times (Fig. 7d–f).

For conductive/isolated faults (Fig. 7a, d), the seismicity rate increases on the fault ($x_3 < -0.2$ km) are due to: (1) poroelastic extension inducing early seismicity and (2) post-injection diffusion of pore pressure causing later seismicity. For conductive/connected faults (Fig. 7b, e), large increases in the seismicity rate ($\log_{10} R > 4$ for these parameters) are observed throughout the fault zone due to rapid diffusion of pore pressure into the fault. The maximum seismicity rate and its duration also depend on the characteristic decay time, t_a, as discussed in

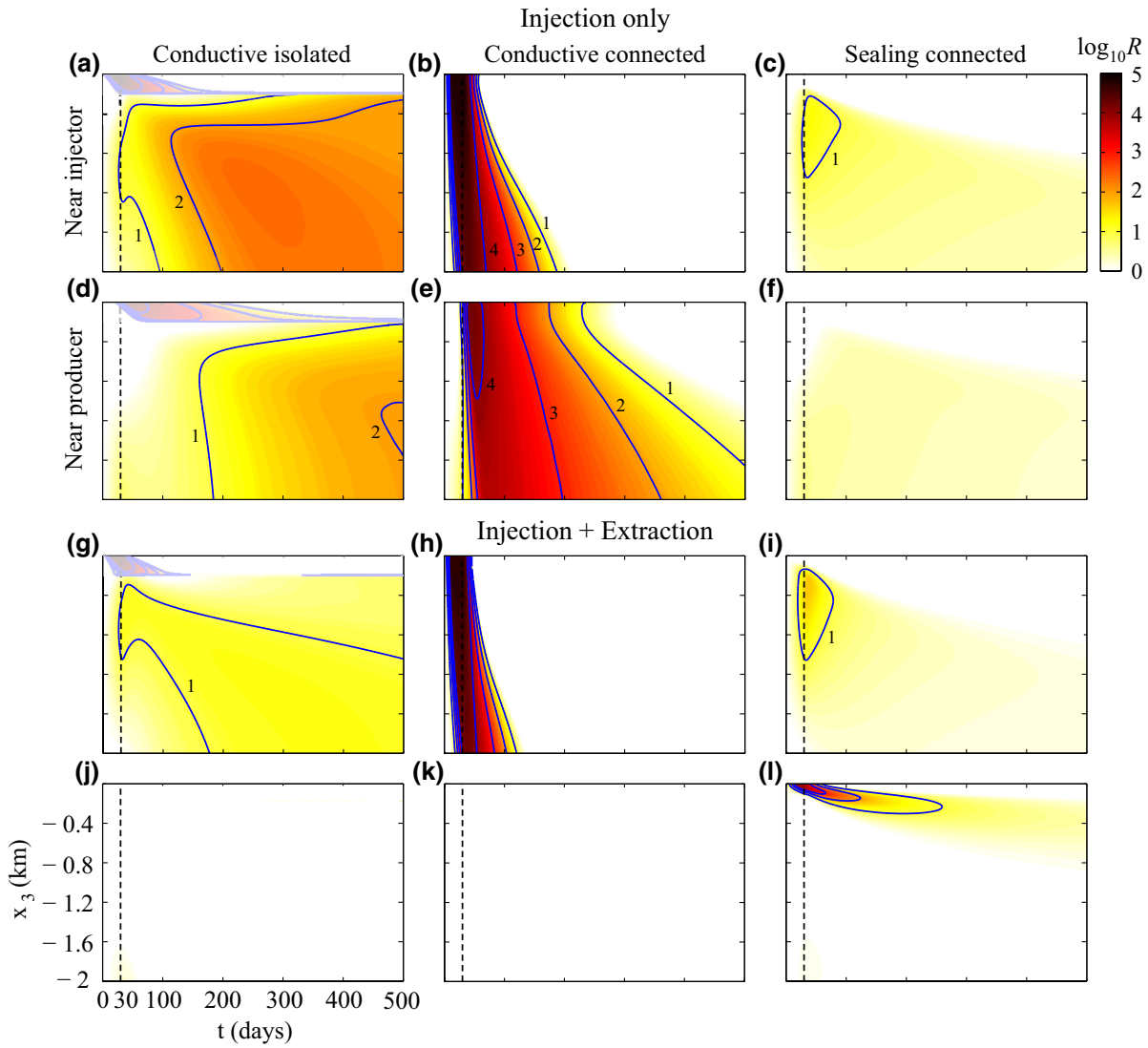

Figure 7
Seismicity rate $R(t)$ on faults near (**a**–**c**, **g**–**i**) injector and (**d**–**f**, **j**–**l**) producer for three types of basement faults. For reference, we obtain $R(t)$ for the case of no extraction (**a**–**f**). *Dash line* indicates the end of well operations ($\Delta t = 30$ days)

Chang and Segall (2016). For sealing faults (Fig. 7c, f), low permeability inhibits direct diffusion into the fault. Pore-pressure buildup in adjacent basements leads to the compression of the shallow fault ($-0.1 < x_3 < 0$ km), restraining seismicity. On the other hand, poroelastic extension of the storage formation can contribute to modest increases in the seismicity rate ($\log_{10} R \sim 1$ for these parameters) on the deeper fault zone ($x_3 < -0.1$ km). Note that the magnitude and onset of the seismicity on the faults are determined by the injection scenario (time and rate), location of the faults, and hydraulic and mechanical properties of the faults and bounding sequences (Chang and Segall 2016).

Fluid extraction diminishes injection-induced pore pressures within the storage reservoir, reducing diffusion into the basement, and potentially stabilizing conductive fault zones. Near the injector (Fig. 7g, h), the diminished perturbation in pore pressure and poroelastic stress reduces the magnitude and duration

of R on conductive faults. Near the producer (Fig. 7j, k), both poroelastic compression ($f\Delta\sigma_n < 0$) and pore-pressure depletion ($f\Delta p < 0$) prevent seismicity on the faults.

For the sealing fault, fluid extraction perturbs the stress states solely by poroelastic stressing. Near the injector (Fig. 7i), increased seismicity rate develops along the deep fault zone with rapid decay (compared to Fig. 7c), due to amplified poroelastic extension driven by pore-pressure declines near the producing well. Near the producer (Fig. 7l), no seismicity is generated on the deep fault zone, since production-induced compression inhibits normal faulting. Instead, an increase in seismicity rate ($\log_{10} R > 3$ for these parameters) occurs on the shallow fault zone beneath the reservoir ($-0.6 < x_3 < 0$ km), because pore-pressure depletion in the surrounding basement rocks unclamps the shallow fault zone (refer to Fig. 4c and Fig. 6f).

The effect of fluid extraction on induced seismicity can be understood by looking at the different components of the Coulomb stress change $\Delta\tau$: $\Delta\tau_s$, $f\Delta\sigma_n$, and $f\Delta p$. Figure 8 shows the temporal evolution of these components at a depth of 0.6 km for three types of faults (top three rows) and a depth of 0.1 km for the sealing fault (bottom row).

For the conductive/isolated fault near the injector (Fig. 8a), poroelastic extension ($f\Delta\sigma_n > 0$, blue line) leads to an increase in $\Delta\tau$ (red line) prior to shut-in, while post shut-in diffusion into the fault ($f\Delta p > 0$, orange line) maintains $\Delta\tau$ at later times (Fig. 7g). Near the producer (Fig. 8e), both poroelastic compression ($f\Delta\sigma_n < 0$) during well operations and post shut-in depletion from the fault ($f\Delta p < 0$) reduces $\Delta\tau$, preventing seismicity along the isolated/conductive fault (refer to Fig. 7j).

For the conductive/connected fault, pore-pressure diffusion dominates fault stability, such that $\Delta\tau \approx f\Delta p$. The maximum value of $|\Delta\tau|$ is obtained after shut-in. Near the injector (Fig. 8b), the increase in $\Delta\tau$ induces seismicity throughout the fault zone (refer to Fig. 7h). Near the producer (Fig. 8f), the decrease in $\Delta\tau$ inhibits seismicity (refer to Fig. 7k).

For the sealing fault, the increase in seismicity occurs only due to poroelastic stressing. Note that pore-pressure perturbations still develop due to poroelastic changes in mean normal stress, rather than diffusion. Near the injector, poroelastic extension of the storage formation increases $\Delta\sigma_n$, and to a lesser extent $\Delta\tau_s$, on the deep fault (Fig. 8c), resulting in an increase in $\Delta\tau$, and potentially triggering seismicity (refer to Fig. 7i). On the shallow fault (Fig. 8d), poroelastic compression, induced by pressurization of basement rocks adjacent to the fault, clamps the fault resulting in negative $\Delta\tau$, and stabilizing the fault zone after shut-in.

Near the producer, on the deep fault (Fig. 8g), extraction-induced contraction of the formation reduces shear and normal stresses ($\Delta\tau_s < 0$ and $\Delta\sigma_n < 0$), which gives only modest changes in the seismicity rate at a depth of 0.6 km. However, on the shallow fault (Fig. 8h) that is bounded by basement rocks with decreased pore pressure, poroelastic extension increases $\Delta\tau$, favoring the slip on normal faults ($\Delta\tau_s > 0$), and potentially increasing the seismicity rate at a depth of 0.1 km (refer to Fig. 7l).

4. Summary and Conclusion

Simultaneous injection and extraction of fluids diminishes pore pressure perturbations relative to injection-only scenarios. In particular, extraction decreases the volume of crust in which pore pressures exceed a given threshold. Nevertheless, the maximum extent of the disturbance occurs after shut-in, emphasizing the need for post-injection monitoring.

Vertical diffusion of pore pressure into basement rocks can affect the stability of basement faults, even though it reduces the pressurized volume within the target reservoir. Fluid extraction retards the lateral and vertical propagation of the pressure “front”, and thus may reduce the direct impact of pore pressure diffusion on the stability of basement faults.

Our calculations confirm that poroelastic stresses can be transmitted to basement faults, potentially inducing seismicity, even without direct pore-pressure diffusion. For conductive faults hydraulically isolated from the storage reservoir, the change in Coulomb stress is controlled by basement diffusivity and injection history. If faults are hydraulically connected to the target reservoir, rapid pore-pressure diffusion into/out of the fault zones leads to large increases (decreases) in Coulomb stress near injector (producer), such that $\Delta\tau \approx f\Delta p$. For isolated or

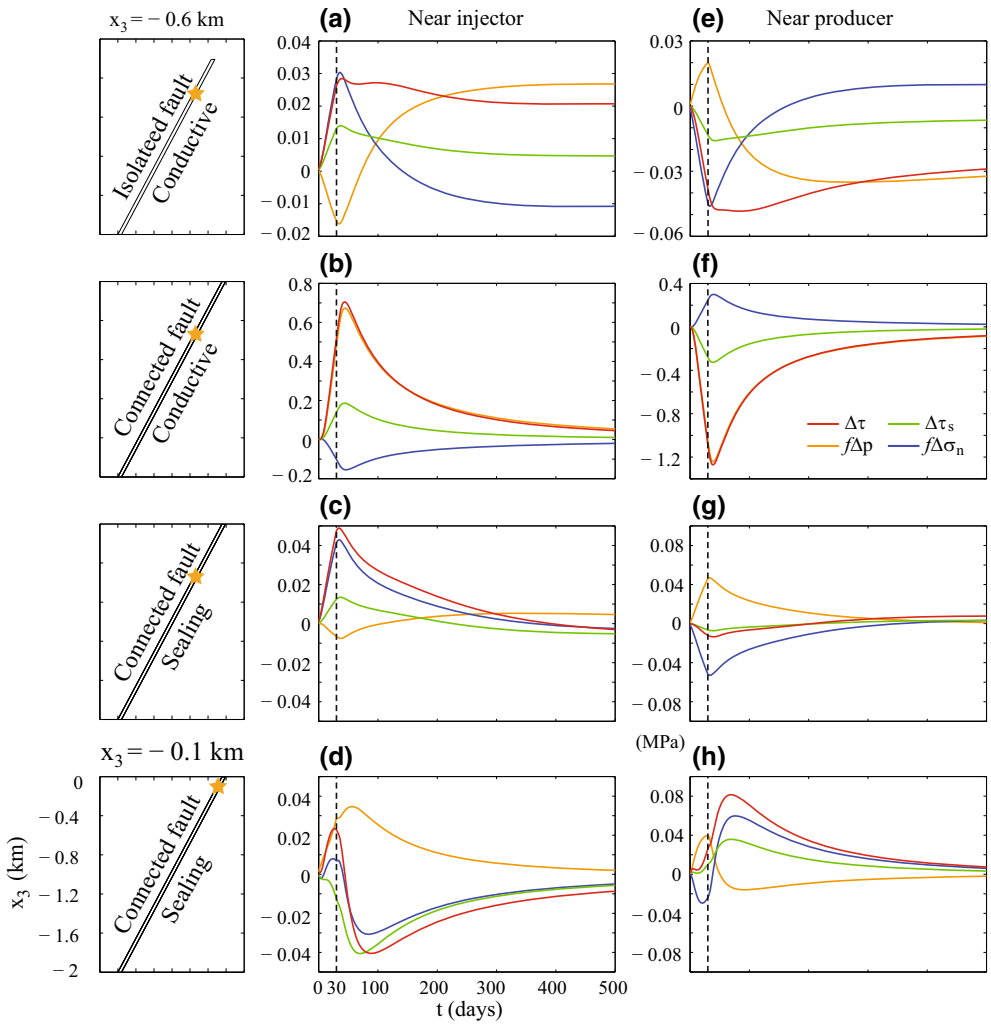

Figure 8
Components of Coulomb stress change $\Delta\tau$ on faults near (**a**–**c**) injector and (**e**–**g**) producer at $x_3 = -0.6$ km and near (**d**) injector and (**h**) producer at $x_3 = -0.1$ km: **a**, **e** conductive/isolated fault, **b**, **f** conductive/connected fault, and **c**–**d**, **g**–**h** sealing fault. Fault geometries are shown in a *left column*; pore pressure and stresses computed at *orange star points*. *Dash line* indicates the end of well operations ($\Delta t = 30$ days)

sealing faults, direct pore-pressure diffusion is inhibited, but elevated (depleted) pore pressure in the surrounding basement creates pore pressure gradients which generate poroelastic stresses that can influence fault stability.

Our results confirm that induced seismicity can occur on basement faults by two mechanisms: (1) direct diffusion of pore pressure and (2) indirect poroelastic stressing. As expected, the largest seismicity rates are predicted on connected/conductive faults due to direct pore-pressure diffusion. Smaller increases in seismicity rate can occur on isolated/conductive faults, and sealing faults, due solely to poroelastic stressing.

Fluid extraction significantly reduces seismicity rates on conductive faults, either hydraulically isolated or connected, by mitigating the pore-pressure perturbation. For sealing faults, fluid extraction can cause larger seismicity rates by enhancing poroelastic stressing. Near injectors fluid extraction enhances poroelastic extension of deep basement rocks, resulting in larger seismicity rates along the deep,

sealing normal faults. Near the producer poroelastic extension of the shallow basement can cause considerable increases in seismicity rate on shallow, sealing, normal faults. Details depend on fault geometry, injection/extraction parameters, background stressing rate and friction parameters. Importantly, these processes can be modeled, given sufficient information about the sub-surface.

Acknowledgments

This work was Supported by the Stanford Center for Induced and Triggered Seismicity (SCITS). The authors are grateful to the reviewers of this paper for their constructive comments as well.

References

B. Bennion and S. Bachu. Relative permeability characteristics for supercritical CO_2 displacing water in a variety of potential sequestration zones. SPE Annual Technical Conference and Exhibition, 2005.

P. E. S. Bergmo, A. A. Grimstad, and E. Lindeberg. *Simultaneous CO_2 injection and water production to optimize aquifer storage capacity*. Int. J. Greenh. Gas Con.,*5* (3): 555–564, 2011. doi:10.1016/j.ijggc.2010.09.002.

M. A. Biot. *General theory of three-dimensional consolidation*. J. Appl. Phys., *12*: 155–164, 1941.

J. T. Birkholzer, A. Cihan, and Q. L. Zhou. *Impact-driven pressure management via targeted brine extraction: Conceptual studies of CO_2 storage in saline formations*. Int. J. Greenh. Gas Con., *7*: 168–180, 2012. doi:10.1016/j.ijggc.2012.01.001.

S. E. Buckley and M. C. Leverett. *Mechanism of fluid displacement in sands*. Trans. AIME, *146*: 107–116, 1942. doi:10.2118/942107-G.

T. A. Buscheck, Y. Sun, M. Chen, Y. Hao, T. J. Wolery, W. L. Bourcier, B. Court, M. A. Celia, S. J. Friedmann, and R. D. Aines. *Active CO_2 reservoir management for carbon storage: Analysis of operational strategies to relieve pressure buildup and improve injectivity*. Int. J. Greenh. Gas Con., *6*: 230–245, 2012. doi:10.1016/j.ijggc.2011.11.007.

K. W. Chang and P. Segall. *Injection induced seismicity on basement faults including poroelastic stressing*. J. Geophys. Res. Solid Earth, *121*(4): 2708–2726, 2016. doi:10.1002/2015JB012561.

K. W. Chang, M. A. Hesse, and J.-P. Nicot. *Reduction of lateral pressure propagation due to dissipation into ambient mudrocks during geological carbon dioxide storage*. Water Resour. Res., *49* (5): 2573–2588, 2013. doi:10.1002/wrcr.20197.

Q. Chen and A. Nur. *Pore fluid pressure effects in anisotropic rocks: Mechanisms of induced seismicity and weak faults*. Pure Appl. Geophys., *139*(3–4): 463–479, 1992.

COMSOL Multiphysics. COMSOL Multiphysics User's Guide. COMSOL AB, Burlington, Mass., 2014.

B. Court, M.A. Celia, J.N. Nordbotten, and T.R. Elliot. *Active and integrated management of water resources throughout CO_2 capture and sequestration operations*. Energy Procedia, *4*: 4221–4229, 2011. doi:10.1016/j.egypro.2011.02.370.

J. H. Dieterich. *A constitutive law for rate of earthquake production and its application to earthquake clustering*. J. Geophys. Res. Solid Earth, *99*(B2): 2601–2618, 1994. doi:10.1029/93JB02581.

K. Dreij, Q. A. Chaudhry, B. Jernstrom, R. Morgenstern, and M. Hanke. *A method for efficient calculation of diffusion and reactions of lipophilic compounds in complex cell geometry*. PLoS ONE, *6* (8): 1–18, 2011.

W. L. Ellsworth. *Injection-induced earthquakes*. Science, *341*(6142), 2013. doi:10.1126/science.1225942.

C. Frohlich, W. L. Ellsworth, W. A. Brown, M. Brunt, J. H. Luetgert, T. MacDonald, and S. Walter. *The 17 May 2012 M4.8 earthquake near Timpson, east Texas: An event possibly triggered by fluid injection*. J. Geophys. Res. Solid Earth, *119*: 581–593, 2014. doi:10.1002/2013JB010755.

J. H. Healy, W. W. Rubey, D. T. Griggs, and C. B. Raleigh. *The Denver earthquakes*. Science, *161* (3848): 1301–1310, 1968. doi:10.1126/science.161.3848.1301.

J. E. Heath, S. A. McKenna, T. A. Dewers, J. D. Roach, and P. H. Kobos. *Mutiwell CO_2 injectivity: Impact of boundary conditions and brine extraction on geological CO_2 storage efficiency and pressure buildup*. Environ. Sci. Technol., *48*: 1067–1074, 2014. doi:10.1021/es4017014.

M. J. Hornbach, H. R. DeShon, W. L. Ellsworth, B. W. Stump, C. Hayward, C. Frohlich, H. R. Oldham, J. E. Olson, M. B. Magnani, C. Brokaw, and J. H. Luetgert. *Causal factors for seismicity near Azle, Texas*. Nature communications, *6* (6728): 1067–1074, 2015. doi:10.1038/ncomms7728.

S. Horton. *Disposal of hydrofracking waste water fluid by injection into subsurface aquifers triggers earthquake swarm in Central Arkansas with potential for damaging earthquake*. Seismol. Res. Lett., *83*(2): 250–260, 2012. doi:10.1785/gssrl.83.2.250.

S. A. Hosseini and J. P. Nicot. *Scoping analysis of brine extraction/re-injection for enhanced CO_2 storage*. Greenh. Gases Sci. Technol., *2*: 172–184, 2012.

T. J. R. Hughes. The Finite Element Method. Dover Publications, 2000.

K. M. Kerenan, H. M. Savage, G. A. Abers, and E. S. Cochran. *Potentially induced earthquakes in Oklahoma, USA: Links between wastewater injection and the 2011 M_w 5.7 earthquake sequence*. Geology, 41: 699–702, 2013. doi: 10.1130/G34045.1.

K. M. Kerenan, M. Weingarten, G. A. Abers, B. Bekins, and S. Ge. *Sharp increase in central Oklahoma seismicity since 2008 induced by massive wastewater injection*. Science, *345*(6159): 448, 2014. doi:10.1126/science.1255802.

W. Y. Kim. *Induced seismicity associated with fluid injection into a deep well in Youngstown, Ohio*. J. Geophys. Res. Solid Earth, *118*(7): 3506–3518, 2013. doi:10.1002/jgrb.50247.

S. Kim and S. Hosseini. *Above-zone pressure monitoring and geomechanical analyses for a field-scale CO_2 injection project, Cranfield, MS*. Greenh. Gas Sci. Technol., *4*: 81–98, 2013.

H. Liu, Z. Hou, P. Were, X. Sun, and Y. Gou. *Numerical studies on CO_2 injection-brine extraction process in a low-medium temperature reservoir system*. Environ. Earth Sci., *73* (11): 6839–6854, 2015. doi:10.1007/s12665-015-4086-3.

B. Metz, O. Davidson, H. De Coninck, M. Loos, and L. Meyer. Special Report on Carbon Capture and Storage. Cambridge University Press, Cambridge, U.K., and New York, NY, U.S.A., 2005.

J.-P. Nicot, S. D. Hovorka, and J.-W. Choi. I*nvestigation of water displacement following large CO_2 sequestration operations*. Energy Procedia, *1*(1): 4411–4418, 2009. DOI: 10.1016/j.egypro.2009.02.256.

C. B. Raleigh, J. H. Healy, and J. D. Bredehoeft. *An experiment in earthquake control at Rangely, Colorado*. Science, *191*(4233): 1230–1237, 1976. doi:10.1126/science.191.4233.1230.

J. R. Rice and M. P. Cleary. *Some basic stress diffusion solutions for fluid-saturated porous media with compressible constituents*. Rev. Geophys., *14*(2): 227–241, 1976. doi:10.1029/RG014i002p00227.

J. L. Rubinstein and A. B. Mahani. *Myths and facts on wastewater injection, hydraulic fracturing, enhanced oil recovery, and induced seismicity*. Seismol. Res. Lett., *86*(4): 1060–1067, 2015. doi:10.1785/0220150067.

J. Rutqvist, J. Birkholzer, F. Cappa, and C.-F. Tsang. *Estimating maximum sustainable injection pressure during geological sequestration of CO_2 using coupled fluid flow and geomechanical fault-slip analysis*. Energ. Convers. Manage., *48*(6): 1798–1807, 2007.

P. Segall. *Earthquakes triggered by fluid extraction*. Geology, *17*(10): 942–946, 1989.

P. Segall. Earthquake and Volcano Deformation. Princeton University Press, Princeton, NJ, 2010.

P. Segall and S. D. Fitzgerald. *A note on induced stress changes in hydrocarbon and geothermal reservoirs*. Tectonophysics, *289* (1): 117–128, 1998. doi:10.1016/S0040-1951(97)00311-9.

P. Segall, J.-R. Grasso, and A. Mossop. *Poroelastic stressing and induced seismicity near the Lacq gas field, southwestern France*. J. Geophys. Res., *99*(B8): 15423–15438, 1994. doi:10.1029/94JB00989.

P. Segall and S. Lu. *Injection induced seismicity: poroelastic and earthquake nucleation effects*. J. Geophys. Res. Solid Earth, *120* (7): 5082–5103, 2015. doi:10.1002/2015JB012060.

E. Stanislavsky and G. Garven. *The minimum depth of fault failure in compressional environments. Geophys*. Res. Lett., *29*(24): 2155, 2002. doi:10.1029/2002GL016363.

A. L. Stork, J. P. Verdon, and J.-M. Kendall. *The microseismic response at the In Salah Carbon Capture and Storage (CCS) site*. Int. J. Greenh. Gas Con., *32*: 159–171, 2015. doi:10.1016/j.ijggc.2014.11.014.

J. E. Streit and R. R. Hillis. *Estimating fault stability and sustainable fluid pressures for underground storage of CO_2 in porous rock*. Energy, *29*(9): 1445–1456, 2004.

P. Talwani and S. Acree. *Pore pressure diffusion and the mechanism of reservoir-induced seismicity*. Pure Appl. Geophys., *122*(6): 947–965, 1984.

S. Thibeau and V. Mucha. *Have we overestimated saline aquifer CO_2 storage capacities?* Oil Gas Sci. Technol. - Rev. IFP Energ. Nouvelles, *66*: 81–92, 2011.

J. P. Verdon, J.-M. Kendall, A. L. Stork, R. A. Chadwick, D. J. White, and R. C. Bissell. *A comparison of geomechanical deformation induced by megatonne scale CO_2 storage at Sleipner, Weyburn and In Salah*. Proc. Natl. Acad. Sci., *110*: E2762–E2771, 2013. doi:10.1073/pnas.1302156110.

H. F. Wang. Theory of Linear Poroelasticity. Princeton University Press, Princeton, NJ, 2000.

H. J. Welge, E. F. Johnson, A. L. Hicks, and F. H. Brinkman. *An analysis for predicting the performance of cone shaped reservoirs receiving gas or water injection*. J. Petrol. Technol., *14*(8): 894–898, 1962. doi:10.2118/294-PA.

J. P. Willson, R. J. Lunn, and Z. K. Shipton. *Simulating spatial and temporal evolution of multiple wing cracks around faults in crystalline basement rocks*. J. Geophys. Res. Solid Earth, *112* (B08408), 2007. doi:10.1029/2006JB004815.

Y. Zhang, M. Person, J. Rupp, K. Elett, M. A. Celia, C. W. Gable, B. Bowen, J. Evans, L. Bandilla, P. Mozley, T. Dewers, and T. Elliot. *Hydrogeologic controls on induced seismicity in crystalline basement rocks due to fluid injection into basal reservoirs*. Ground Water, *51*(4): 525–538, 2013. doi:10.1111/gwat.12071.

M. D. Zoback and S. M. Gorelick. *Earthquake triggering and large-scale geologic storage of carbon dioxide*. Proc. Natl. Acad. Sci., *109*(26): 10164–10168, 2012. doi:10.1073/pnas.1202473109.

(Received January 11, 2016, revised May 14, 2016, accepted May 17, 2016)